Tailoring the electronic states of Pt by atomic layer deposition of Al_2O_3 for enhanced CO oxidation performance: Experimental and theoretical investigations

Siyuan Hu, Mingzhen Huang, Jingru Li, Jinxin He, Kaiji Xu, Xiaoping Rao, Dongren Cai, Guowu Zhan [*],[1]

College of Chemical Engineering, Integrated Nanocatalysts Institute (INCI), Institute of Advanced Carbon Conversion Technology, Huaqiao University, 668 Jimei Avenue, Xiamen, Fujian 361021, PR China

ARTICLE INFO

ABSTRACT

Herein, atomic layer deposition (ALD)-Al_2O_3 films were applied as a medium to modulate the electronic states of the supported Pt. Based on the sacrificial template of ZIF-67, the ternary $Co_3O_4/Pt/Al_2O_3$ catalyst exhibited better performance in catalytic CO oxidation than the binary Co_3O_4/Pt catalyst. Both experimental and calculation results indicate the existence of charge transport between the Pt and the ALD-Al_2O_3 films, leading to electron-rich Pt, enhanced O_2 affinity, and reduced activation energy. Interestingly, the oxidation resistance of Pt nanoparticles was visualized when annealing $Co_3O_4/Pt/Al_2O_3$ catalyst at high temperatures. Mechanism studies indicate the typical LH mechanism occurred in CO oxidation, showing that the co-adsorbed CO and O_2 could be converted to carbonate-type *OCOO intermediates via low energy barriers. At low temperatures, CO_2 was mainly produced by the lattice oxygen-mediated M-vK mechanism based on isotope labeling experiments. Our findings provide an alternative way to regulate the electronic states of noble metals by the ALD technique.

1. Introduction

The catalytic oxidation of carbon monoxide (CO) to carbon dioxide (CO_2) has been extensively studied as a prototypical heterogeneous catalytic reaction, which is critical to many industrial applications [1–3]. For instance, in the field of proton exchange membrane fuel cells (PEMFC), it can remove a tiny amount of CO from H_2-containing gas streams by preferential oxidation of CO (PROX), which is of great interest for PEMFC applications [4,5]. In exhaust gas treatment from gasoline-fueled automobiles, catalytic oxidation of CO is regarded as a key technology to solve increasingly severe environmental problems [6–9].

Among the various catalysts, Pt-based catalysts have been extensively utilized in the catalytic CO oxidation reaction. Considering the scarcity and high cost of Pt, it is crucial to efficiently exert the catalytic activity of Pt under various complicated catalytic conditions. Therefore, a great deal of effort has been devoted to maximizing the catalytic activity of Pt sites by controlling the geometric structures (particle size and shape) [10], chemical compositions [11], electronic states [12],

metal-support interactions [13], and so forth. Particularly, many in-depth studies have been carried out to analyze the relationship between the electronic state of Pt and its catalytic activity in CO oxidation reactions. For instance, Beniya et al. investigated that Pt nanoparticles (NPs) with an electron-deficient state had a lower affinity of O_2, resulting in the low activity of CO oxidation [14]. In comparison, the electron-rich state of Pt produces favorable adsorption and activation behavior for O_2, thus improving the catalytic activity of CO oxidation [15,16]. Benchmarks of the electronic state of Pt catalysts (electron-rich or electron-deficient) versus half- and full-conversion temperatures of CO (T_{50} and T_{100}) are summarized in Table S1. It seems that the effect of Pt electronic states on the activity of CO oxidation remains debated. Those catalysts are objective differences in metal loading contents, supports, and even pretreatment conditions, resulting in diverse surface and interfacial properties. However, there is no doubt that the electronic state of Pt is one of the significant factors affecting the activity of CO oxidation. Therefore, it would be feasible and effective to enhance the CO oxidation performance by adjusting the electronic state of Pt NPs.

So far, many strategies have been reported for tuning the electronic

---
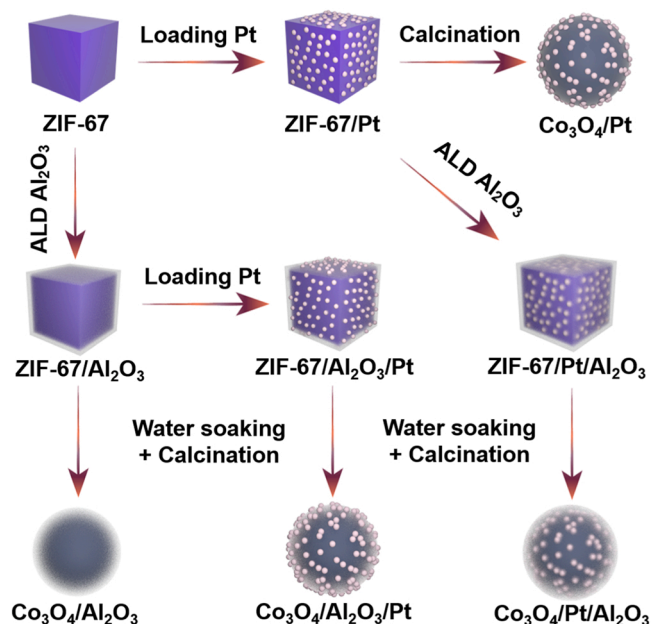
Scheme 1. Schematic illustration of the fabrication routes of Co_3O_4/Pt, Co_3O_4/Al_2O_3, $Co_3O_4/Al_2O_3/Pt$, and $Co_3O_4/Pt/Al_2O_3$ catalysts deriving from ZIF-67 nanocubes as sacrificing templates. Notes: the water-soaking treatment proceeded at room temperature under stirring for 45 min and the calcination treatment was conducted at 300 °C in the air for 5 h.

state of Pt. For example, by modulating the photothermal effect, it is possible to flexibly alter the electronic density on the surface of Pt nanocrystals and improve the ability of Pt to generate singlet oxygen [17]. Adjusting the diverse crystal facets of metal oxides will also result in different dispersions and electronic injections of Pt [18]. In addition, one of the key strategies is to immobilize Pt NPs on redox-active support to form electronic metal-support interactions (EMSIs) and unique interfaces. Electron transfer from support can shift the *d*-band center of metal, which could influence the adsorption and desorption of molecules [19]. By comprehensively comparing these methods, immobilizing metals on supports can provide diverse opportunities for tuning the electronic structure of the metallic NPs, which is determined by the diversity of supports [20]. The T_{50} and T_{100} of Pt catalysts on different supports for CO oxidation are summarized in Table S2. Obviously, Pt catalysts have lower T_{50} and T_{100} when loaded on redox-active supports (CeO_2, TiO_2, CoO_x, FeO_x, etc.) due to the ability of the redox carrier to generate active oxygen species, which provides a more favorable chemical environment for CO oxidation reactions.

On the other hand, atomic layer deposition (ALD) is a nano-fabrication technology that can precisely control the thickness and size of the deposition films at the atomic scale, which has been widely used in the encapsulation of semiconductor materials [21,22]. In the field of heterogeneous catalysis, ALD technology has been applied to deposit oxide films to protect metal particles from sintering and agglomeration by adjusting the number of cycles and deposition conditions [23]. For instance, the addition of ALD-MnO_x can improve the durability of the Pt/Al_2O_3 catalyst and reduce the agglomeration of Pt particles as annealing at 800 °C [24]. Nonetheless, little research has been conducted on tuning the electronic state of Pt by ALD techniques, and the intrinsic mechanism of how ALD deposits affect the electronic state of Pt is still unclear.

Accordingly, herein, the ALD deposited Al_2O_3 film was used to modify the electronic states of Pt NPs which were pre-loaded on porous Co_3O_4 support (e.g., Co_3O_4/Pt, Co_3O_4/Al_2O_3, $Co_3O_4/Al_2O_3/Pt$, and $Co_3O_4/Pt/Al_2O_3$). The four different catalysts were prepared by adjusting the sequence of ALD-deposited Al_2O_3 films and Pt-loading steps (see Scheme 1). In particular, the redox-active Co_3O_4 support

was fabricated by using ZIF-67, a common zeolite-like metal-organic framework (MOF), as a sacrificial template during water-soaking and calcination treatments. It was found that the obtained ternary $Co_3O_4/Pt/Al_2O_3$ catalysts can completely convert CO at 100 °C ($T_{100} = 100 °C$) and have desirable anti-sintering stability and oxidation resistance properties even after being annealed at 600 °C. X-ray photoelectron spectroscopy (XPS), CO chemisorption, and density functional theory (DFT) calculations were applied to verify the effect of Al_2O_3 film on the electronic state of Pt NPs. The results unambiguously indicate that the electron-donating effect of Al_2O_3 allows Pt to become electron-rich states, giving the catalyst a stronger O_2 affinity, which is likely to be the reason for the better performance in the CO oxidation reaction, as compared to the catalysts without coating ALD-Al_2O_3 films.

2. Experimental section

2.1. Chemicals

The following chemicals were used as received: 2-methylimidazole (2-MeIm, 98%, Aladdin), cobalt (II) nitrate hexahydrate (98.5%, XiLong Scientific Co., Ltd), hexadecyltrimethylammonium chloride (CTAC, 99%, Sinopharm Chemical Reagent Co., Ltd), tetrabutylammonium borohydride (R-NBH_4, 95%, Adamas), chloroplatinic acid hydrate (99.9%, Adamas), tri-methyl aluminum (TMA, 99.99%, Adamas), methanol (99.5%, Adamas), ethanol (99.7%, Adamas), and deionized water (made by a water filtration system in our laboratory).

2.2. Synthesis of ZIF-67 nanocubes

The synthesis of ZIF-67 nanocubes was conducted at room temperature. Firstly, 6 mL of $Co(NO_3)_2$ (50 g/L, 0.172 M) aqueous solution was added to 68 mL of water containing 3.6 g of 2-MeIm. After stirring for 2 min, 8 mL of aqueous CTAC solution (5 wt%) was added to selectively inhibit the growth of ZIF-67 crystals along the (100) direction, resulting in the formation of a cubic shape of ZIF-67 [25]. The above mixture was further stirred for 8 h, and the resultant purple solid (i.e., ZIF-67) was harvested through centrifugation (11000 r/min for 5 min), washing (with ethanol twice), and drying overnight at 60 °C for later use.

2.3. Synthesis of precursor nanomaterials (ZIF-67/Pt, ZIF-67/Al₂O₃, ZIF-67/Al₂O₃/Pt, and ZIF-67/Pt/Al₂O₃)

The in-situ reduction method was applied to loading Pt NPs onto ZIF-67 support based on our previous study [26]. Specifically, 160 mg of ZIF-67 was well dispersed in 40 mL of methanol (by sonication for 1 h and stirring for 1 h). Then 2 mL of H_2PtCl_6 methanolic solution (19.6 mM) was added and stirred for 1 h at room temperature. Subsequently, 10 mL of freshly prepared R-NBH_4 methanolic solution (0.25 M) was injected into the above mixture. After stirring for 1 h, the product (i.e., ZIF-67/Pt composite) was collected through centrifugation (11000 r/min for 5 min), washing (with ethanol for one time), and drying overnight at 60 °C.

ZIF-67/Al_2O_3 was obtained by directly coating Al_2O_3 film on ZIF-67 in ALD equipment (Angstrom-dep III). Specifically, 160 mg of ZIF-67 was loaded into the sample chamber and subsequently heated to 110 °C, while TMA and H_2O were used as a metal precursor and oxygen source, respectively. TMA and H_2O were held in a stainless-steel bottle, which was kept at 90 °C during the Al_2O_3 ALD coating process. N_2 flow (6 mL/min) was used as inert gas for precursor pulse exposure. The pulse and purge times were set as 1 and 70 s, respectively, for TMA feeding, and 0.5 and 70 s, respectively, for H_2O feeding. The pulse pressure of TMA and H_2O were both 0.09 Pa. The number of ALD cycles was set to 10 times.

Along a similar line, ZIF-67/Al_2O_3/Pt and ZIF-67/Pt/Al_2O_3 can be obtained by using the above-described Pt loading step and ALD-deposited Al_2O_3 step over the synthesized ZIF-67/Al_2O_3 and ZIF-67/Pt
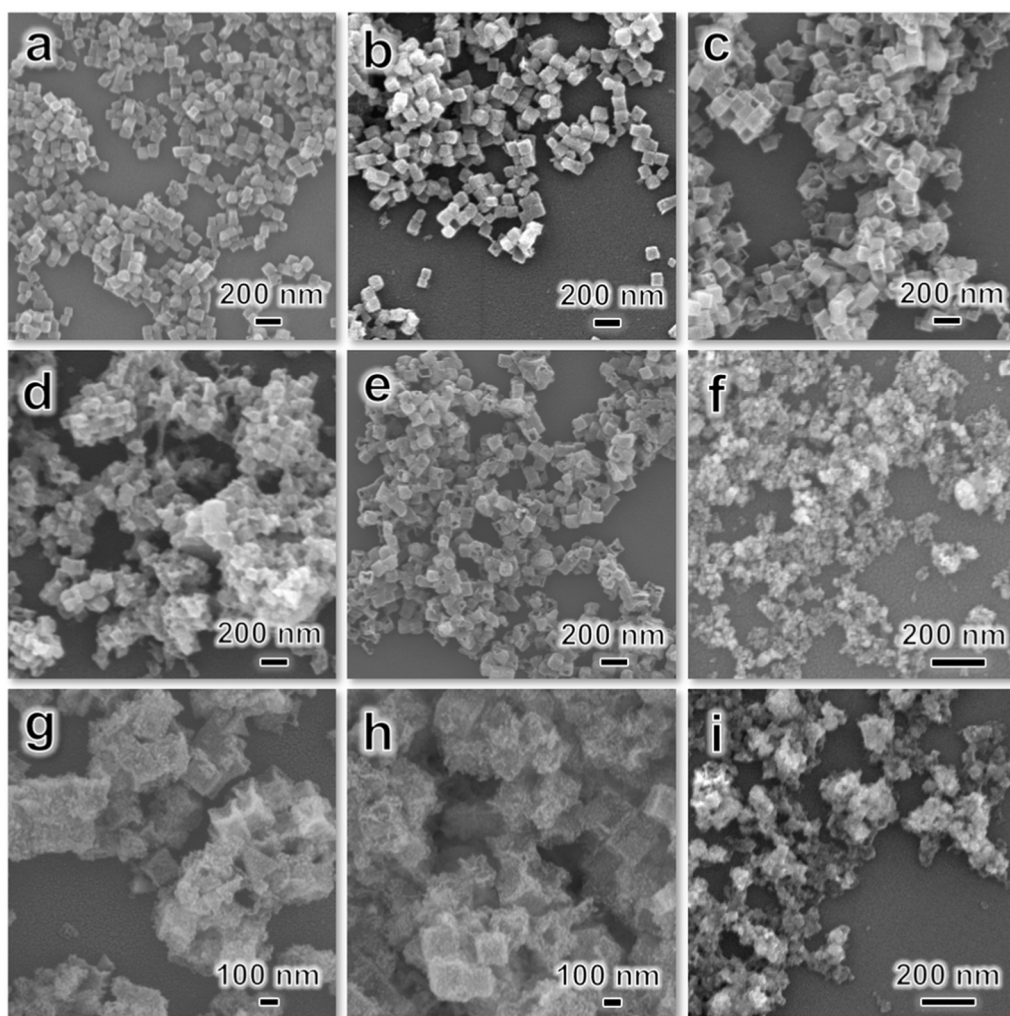
Fig. 1. Representative SEM images of precursor materials and catalyst samples, including (a) ZIF-67, (b) ZIF-67/Pt, (c) ZIF-67/Al$_2$O$_3$, (d) ZIF-67/Al$_2$O$_3$/Pt, (e) ZIF-67/Pt/Al$_2$O$_3$, (f) Co$_3$O$_4$/Pt, (g) Co$_3$O$_4$/Al$_2$O$_3$, (h) Co$_3$O$_4$/Al$_2$O$_3$/Pt, and (i) Co$_3$O$_4$/Pt/Al$_2$O$_3$.

precursors, respectively.

2.4. Synthesis of Co$_3$O$_4$/Pt, Co$_3$O$_4$/Al$_2$O$_3$, Co$_3$O$_4$/Al$_2$O$_3$/Pt, and Co$_3$O$_4$/Pt/Al$_2$O$_3$

Co$_3$O$_4$/Pt, Co$_3$O$_4$/Al$_2$O$_3$, Co$_3$O$_4$/Al$_2$O$_3$/Pt, and Co$_3$O$_4$/Pt/Al$_2$O$_3$ catalysts were obtained by post-treating the precursor nanomaterials (ZIF-67/Pt, ZIF-67/Al$_2$O$_3$, ZIF-67/Al$_2$O$_3$/Pt, ZIF-67/Pt/Al$_2$O$_3$) based on our previous work [25]. Specifically, the above-obtained ZIF-67/Al$_2$O$_3$, ZIF-67/Al$_2$O$_3$/Pt, and ZIF-67/Pt/Al$_2$O$_3$ precursors were soaked in 30 mL of water at room temperature under stirring for 45 min to produce a porous structure due to the etching of ZIF-67 by water. Then the solids were collected through centrifugation (8000 r/min for 5 min) and dried overnight at 60 °C. Subsequently, the water-soaked precursors were calcined at 300 °C in the air for 5 h, to obtain Co$_3$O$_4$/Al$_2$O$_3$, Co$_3$O$_4$/Al$_2$O$_3$/Pt, and Co$_3$O$_4$/Pt/Al$_2$O$_3$ catalysts.

It should be particularly noted that for the ZIF-67/Pt precursors (that is, without ALD-Al$_2$O$_3$), very little solid product was obtained after the water-soaking treatment. The reason may be due to the total decomposition of ZIF-67/Pt precursors in the absence of Al$_2$O$_3$ film. Therefore, the ZIF-67/Pt precursor was directly calcined at 300 °C for 5 h to obtain the Co$_3$O$_4$/Pt catalyst.

2.5. Evaluation of CO catalytic oxidation performance

The CO oxidation performance of the catalysts was evaluated in a fixed bed microreactor using CO feed gas (1% CO, 4% O$_2$, balanced by 95% Ar) at atmospheric pressure. First, 50 mg of catalyst was loaded into a quartz reaction tube and pretreated at 200 °C for 2 h (heating rate of 5 °C/min) under the CO feed gas (20 mL/min). After natural cooling down to room temperature, the reaction temperature was raised again from room temperature to a specific temperature under a heating rate of 2 °C/min under the CO feed gas (20 mL/min). The gas compositions in the outlet of the reactor were measured by online mass spectrometry equipment (Pfeiffer Omistar GSD-320). Calculation details of CO conversion, apparent activation energy, turnover frequency (TOF), and reaction orders with respect to O$_2$ and CO can be found in the Supporting information.

2.6. Characterization methods

The sizes and morphologies of the samples were investigated by scanning electron microscopy (SEM, JSM-5600LV) and transmission electron microscopy (TEM, FEI-F200X) with energy-dispersive X-ray spectroscopy (EDX) as an accessory. The crystallographic information was analyzed by X-ray diffraction (XRD, Rigaku Smart Lab) equipped with a Cu Kα radiation source (λ = 1.5406 Å). The textural properties of the samples were measured using N$_2$ physisorption isotherms at 77 K

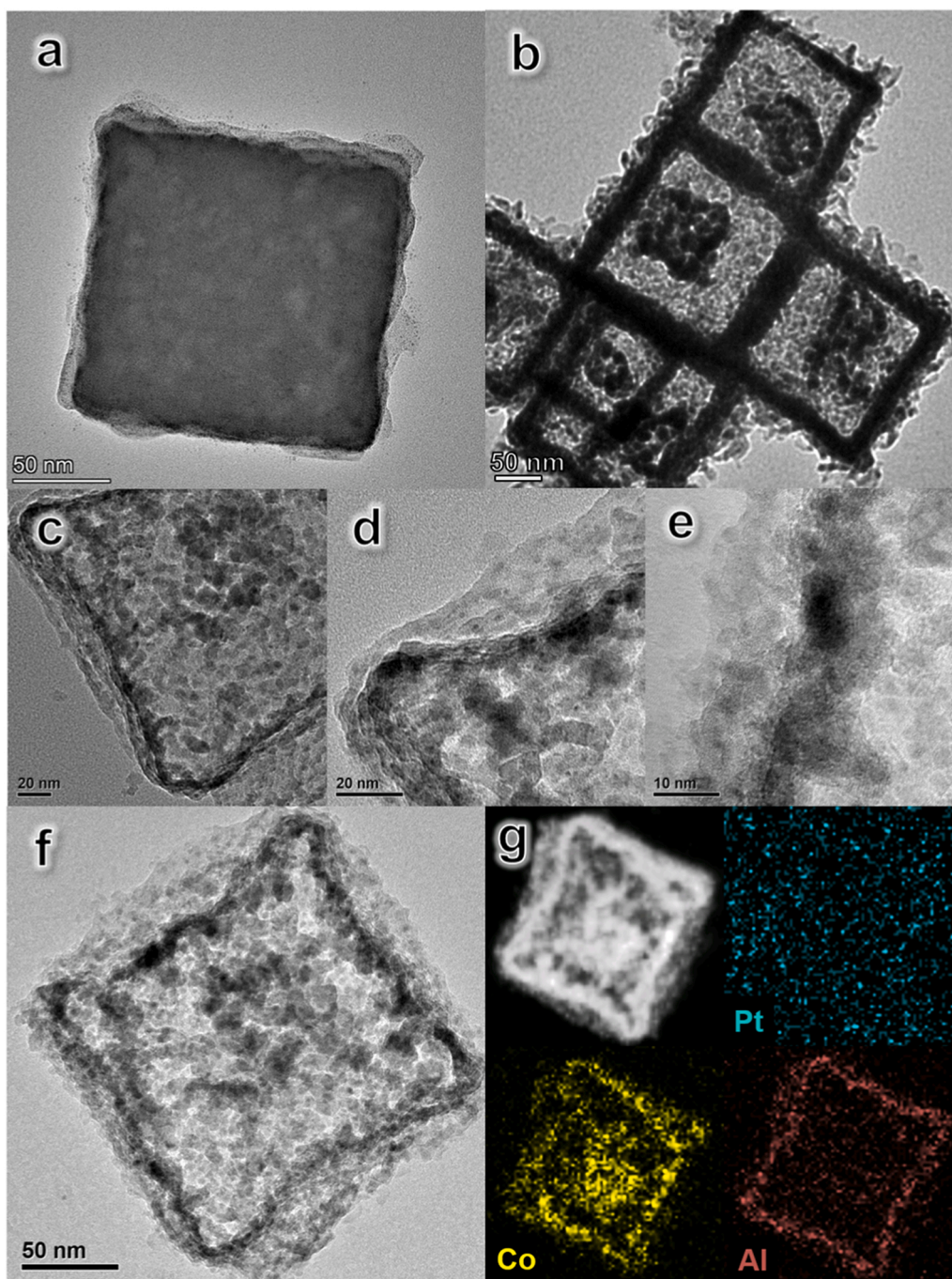**Fig. 2.** Representative TEM images of precursor materials and catalyst samples, including (a) ZIF-67/Pt, (b) Co_3O_4/Al_2O_3/Pt, (c-f) Co_3O_4/Pt/Al_2O_3, and (g) HAADF-STEM images and EDX elemental maps of Co_3O_4/Pt/Al_2O_3. Color codes: cyan, yellow, and red represent Pt, Co, and Al, respectively.

(Quantachrome, Autosorb-iQ). X-ray photoelectron spectra (XPS) were recorded on a K-Alpha spectrometer (Thermo Fischer Scientific). The binding energies were corrected by setting the C *1 s* signal of 284.8 eV as energy calibration. Elemental compositions (e.g., Co, Al, and Pt) in the catalysts were measured by inductively coupled plasma optical emission spectrometry (ICP-OES, Agilent 5110). *In-situ* diffuse reflectance infrared Fourier transform spectroscopy (DRIFTS) was performed using the Thermo Scientific Nicolet iS-50 spectrometer, and the detailed measurement conditions can be found in the Supporting information.

2.7. DFT calculation method

Density functional theory (DFT) calculations were carried out based on the projector-augmented wave method implemented in the Vienna ab initio simulation package (VASP 5.4.1) [27]. The generalized gradient approximation of the Perdew-Burke-Ernzerhof functional was used to calculate exchange-correlation energy with a cutoff energy of 500 eV [28]. The convergence thresholds for atomic energies and forces were set to be 10^{-5} eV and 10^{-2} eV/Å in all calculations of structural optimization. The interactions between periodic models were avoided by setting a vacuum layer larger than 20 Å along the Z direction. In addition, the search for the transition state was performed using the climbing image nudged-elastic band (CI-NEB) algorithm to confirm all transition states have only one imaginary frequency during the CO oxidation calculations via the Langmuir-Hinshelwood mechanism [29].
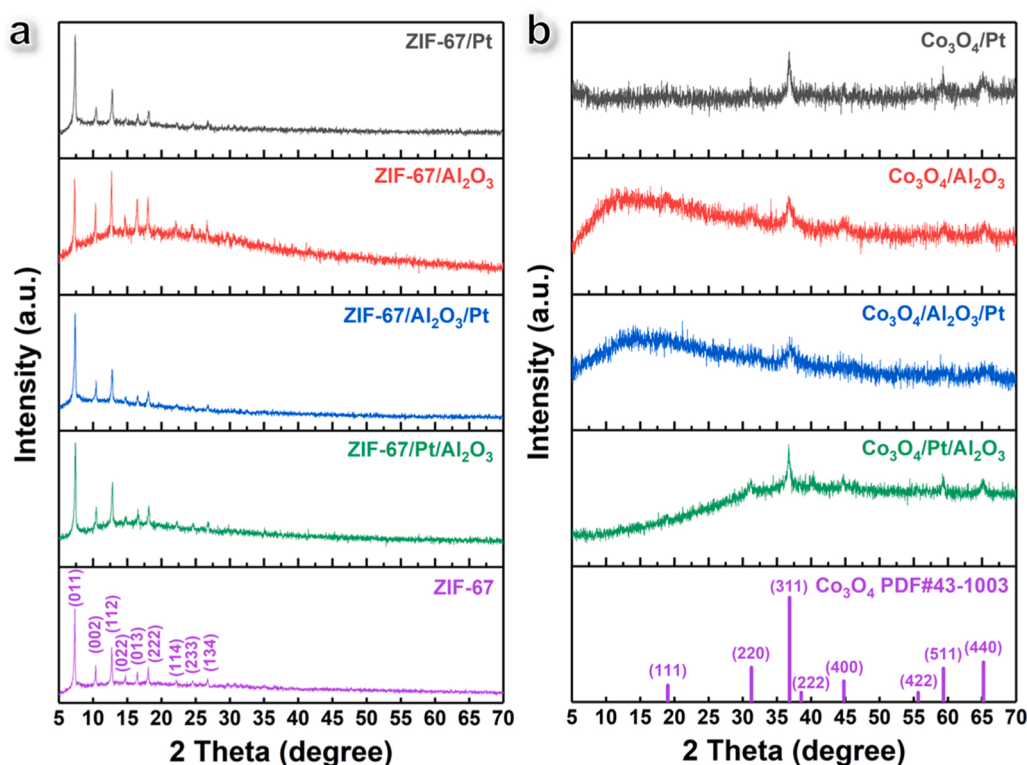
Fig. 3. XRD patterns of (a) ZIF-67-based precursor materials and (b) Co_3O_4-based catalyst samples.

2.8. O_2-TPD and isotope labeling experiment procedure

Oxygen temperature programmed desorption (O_2-TPD) was performed in a chemisorption instrument equipped with a thermal conductivity detector (TCD). First, 50 mg samples were saturated with pure O_2 (30 mL/min) at 30 °C for 1 h before switching to the pure He flow at 50 mL/min and the temperature was maintained at 30 °C for at least 1 h. Then the temperature was raised to 500 °C with a heating rate of 10 °C/min. Isotopic labeling experiments were carried out with a similar instrument. First, 50 mg of fresh-prepared $Co_3O_4/Pt/Al_2O_3$ catalysts were pretreated by pure He flow (50 mL/min) at 200 °C for 2 h to clean the surface and cooled down to 30 °C. Then $^{18}O_2$ gas (30% $^{18}O_2$ in He) was fed to the reactor at a flow rate of 2 mL/min for 5 min. Afterward, pure CO (0.99 mL) was pulsed into the fixed bed reactor using He as the carrier gas. The signals of $C^{16}O_2$ ($m/z = 44$), $^{18}OC^{16}O$ ($m/z = 46$), and $C^{18}O_2$ ($m/z = 48$) in the outlet were measured with mass spectrometry equipment (Pfeiffer Omistar GSD-320).

3. Results and discussion

3.1. Characterizations of precursors and catalysts

Herein, the samples before water-soaking and calcination treatments were denoted as precursor materials, including ZIF-67/Pt, ZIF-67/Al_2O_3, ZIF-67/Al_2O_3/Pt, and ZIF-67/Pt/Al_2O_3. While the samples after water-soaking and calcination treatments were called catalysts being used for CO oxidation performance evaluation, including Co_3O_4/Pt, Co_3O_4/Al_2O_3, Co_3O_4/Al_2O_3/Pt, and Co_3O_4/Pt/Al_2O_3. The representative SEM images of precursor materials and catalysts are exhibited in Fig. 1. Of note, the as-prepared ZIF-67 and all precursor materials were quite uniform in size. The cubic morphology of ZIF-67 was well preserved after ALD-Al_2O_3 and loading Pt NPs (Fig. 1a-e). Because of the presence of water vapor in the ALD-Al_2O_3 coating process, ZIF-67 has poor stability against water vapor leading to the formation of uneven surfaces of ZIF-67/Al_2O_3 and ZIF-67/Pt/Al_2O_3 (Fig. 1c,e). It can also be

observed that the ZIF-67/Al_2O_3, ZIF-67/Al_2O_3/Pt, and ZIF-67/Pt/Al_2O_3 precursors with armored ALD-Al_2O_3 film have a uniform cubic morphology after water soaking and calcination treatments (Fig. 1g-i), while the ZIF-67/Pt without ALD-Al_2O_3 decomposed into the flower-clustered structure after the calcination treatment (Fig. 1f). This indicates the protective effect of Al_2O_3 on maintaining the morphology of ZIF-67 in the post-treatment process (i.e., water soaking and calcination treatments).

The spatial distributions of Pt NPs and ALD-Al_2O_3 film in the precursor materials and catalyst samples were further confirmed using TEM characterization. As can be seen in Fig. 2a, the Pt NPs (size of 2–4 nm) were uniformly dispersed on the ZIF-67 nanocubes. The thickness of the lamellar ALD-Al_2O_3 film was about 2.6 nm (ALD cycle number of 10, Fig. S1). After the water soaking and calcination treatments, the ZIF-67 nanocubes collapsed internally even with the protection of ALD-Al_2O_3 film, forming numerous Co_3O_4 particles as building blocks to maintain the cubic skeleton derived from ZIF-67 (Fig. 2b-f). It should be noted that the transformation of ZIF-67 to Co_3O_4 would partially break the Al_2O_3 encapsulation film, proving that the Al_2O_3 film may not be perfect as covering Pt NPs and Pt NPs are accessible to the reactant gases. Nevertheless, the boundary of the nanocubes was still clearly visible, which further verified the protective effect of the ALD-Al_2O_3 film on the Co_3O_4-based catalysts. Furthermore, EDX elemental maps (Fig. 2g) also demonstrated the uniform distribution of Al elements on the skeleton of the cubic boundary, proving the uniform deposition of Al_2O_3 films.

Crystalline structures of precursor materials and catalyst samples were verified from the XRD patterns. As can be seen in Fig. 3a,b, all precursor materials showed the diffraction peak of the ZIF-67 phases, and the diffraction peaks of Co_3O_4 appeared in all catalysts according to the JCPDS card (No. 43–1003), which was due to the transformation of ZIF-67 to Co_3O_4 during the water-soaking and calcination treatments [25]. The metal node of ZIF-67 was transformed into Co_3O_4 while the organic moiety was totally decomposed. No diffraction peaks of both Pt and Al_2O_3 phases were observed, which may be caused by the uniform dispersion of small-sized Pt NPs and the amorphous state of the
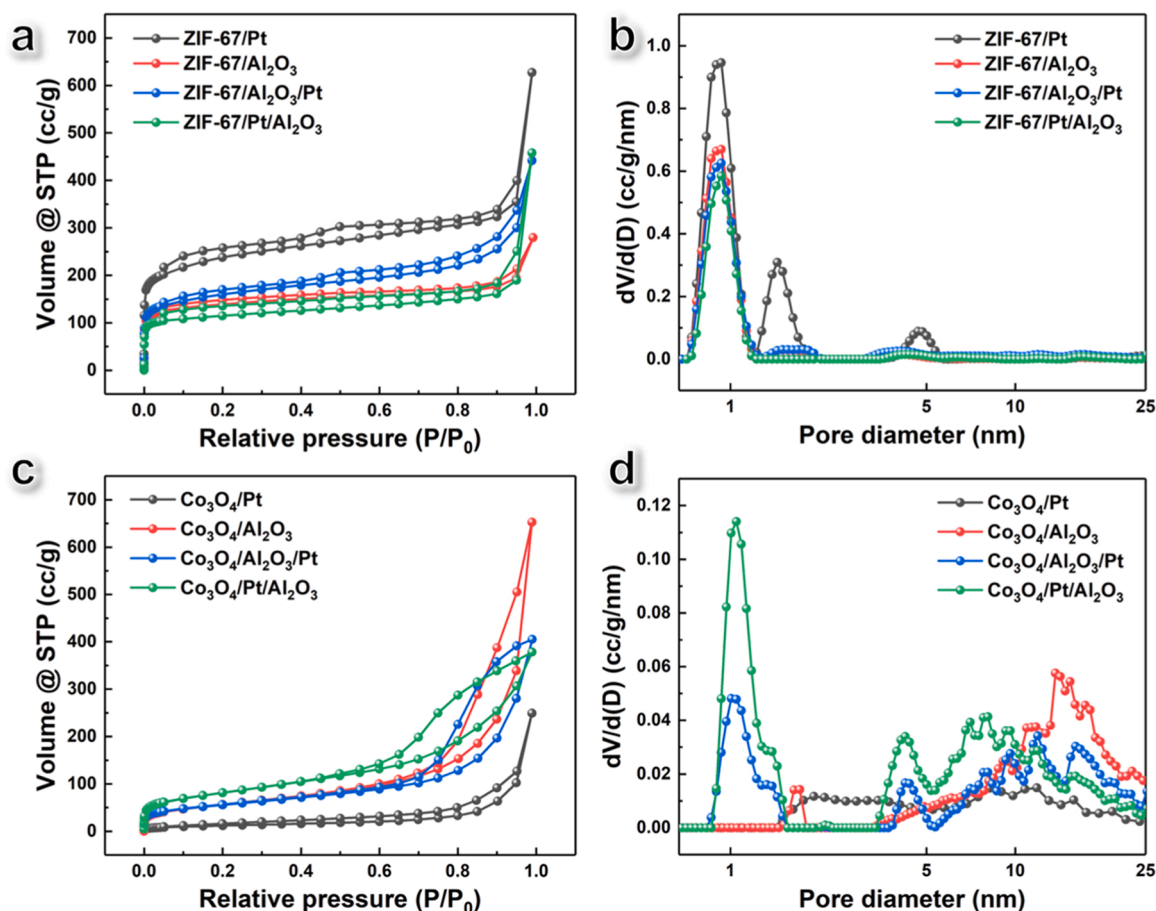
Fig. 4. N_2 physisorption isotherms and pore size distribution curves based on BJH method using adsorption branch of data (a, b) ZIF-67-based precursor materials and (c, d) Co_3O_4-based catalysts. Notes: "STP" in Y-axis means the standard temperature and pressure, and "dV/d(D)" means the differentiation of pore volume to pore diameter, representing the pore area.

ALD-Al_2O_3 films [30].

The textural properties of precursor materials and catalyst samples were studied by N_2 physisorption isotherms (Fig. 4). The textural information of the as-prepared precursors and catalysts can be found in Table S3. The feature of type I isotherms was found in the ZIF-67-based precursor materials reflecting the existence of micropores. Meanwhile, all Co_3O_4-based catalysts showed type IV isotherms with H_4-type hysteresis loop indicating the distribution of mesopore (such as narrow slit-like pores) in the composite materials. In addition, the volume of micropores was reduced by the deposition of ALD-Al_2O_3, indicating the pore-filling effect of Al_2O_3 films due to the intrusion of TMA vapor. Among the four catalyst samples, Co_3O_4/Pt/Al_2O_3 owned the highest specific BET surface area (S_{BET}, 261 m^2/g), indicating the preservation of porous structure by ALD-Al_2O_3 deposition treatment.

ICP-OES was applied to measure the contents of Pt, Co, and Al in the prepared catalysts. As can be seen in Table S4, the Al element was detected in the composite (>15 wt%), proving the successful deposition of the ALD-Al_2O_3 layer. Moreover, Co_3O_4/Al_2O_3/Pt and Co_3O_4/Pt/Al_2O_3 have almost similar Pt content (2.93 and 2.89 wt%), which eliminated their effect on CO oxidation performance (vide infra). Theoretically, the Pt and Co content of Co_3O_4/Pt, Co_3O_4/Al_2O_3/Pt, and Co_3O_4/Pt/Al_2O_3 were consistent, but Co_3O_4/Pt possessed a relatively high Pt content (7.05 wt%) due to the absence of Al_2O_3 layer.

3.2. Evaluation of CO catalytic oxidation performance

The effect of the thickness of the ALD-Al_2O_3 layer on the catalytic performance was first investigated. A series of Co_3O_4/Al_2O_3-x layer/Pt

catalysts (x = 0, 5, 10, 20, 30) were synthesized by controlling the number of ALD cycles. The corresponding catalytic performance data are summarized in Fig. S2, suggesting that the optimal number of deposited layers was 10 layers (see Fig. S2). Subsequently, CO oxidation tests were performed to evaluate the effect of ALD-Al_2O_3 films on the catalytic performance of the supported Pt catalysts. As shown in Fig. 5a, the Co_3O_4/Al_2O_3/Pt (T_{100} = 130 °C) and Co_3O_4/Pt/Al_2O_3 (T_{100} = 100 °C) possessed better catalytic activity than Co_3O_4/Pt (T_{100} = 190 °C). Co_3O_4/Al_2O_3 catalyst without Pt loading showed the poorest activity (T_{100} = 230 °C), reflecting the high activity of Pt sites for the catalytic oxidation of CO. Moreover, the Co_3O_4/Pt/Al_2O_3 even exhibited some activity at room temperature (~20% CO conversion), which was likely caused by CO_2 production from lattice oxygen of Co_3O_4 through the Mars-van Krevelen (M-vK) mechanism (vide infra). The ternary Co_3O_4/Pt/Al_2O_3 exhibited a high TOF of 71.4 h^{-1}, superior to other catalysts reported in the literature [31]. Furthermore, the long-term stabilities of Co_3O_4/Al_2O_3/Pt and Co_3O_4/Pt/Al_2O_3 were studied and compared at 100% and 40% conversion, respectively (Fig. 5b and Fig. S3). It can be seen that both catalysts can maintain full conversion of CO at 200 °C within 50 h. However, at the temperature achieving 40% conversion, the conversion of Co_3O_4/Al_2O_3/Pt slowly decreased by ~15% within 40 h on stream, while Co_3O_4/Pt/Al_2O_3 still maintained a steady state, indicating that Co_3O_4/Pt/Al_2O_3 possesses better activity and stability.

In addition, the activation energies (E_a) of the three supported Pt catalysts were calculated based on the Arrhenius plots. As shown in Fig. 5c, the E_a values increase in the following order: Co_3O_4/Al_2O_3/Pt (15.4 kJ/mol) < Co_3O_4/Pt/Al_2O_3 (19.2 kJ/mol) < Co_3O_4/Pt (48.5 kJ/
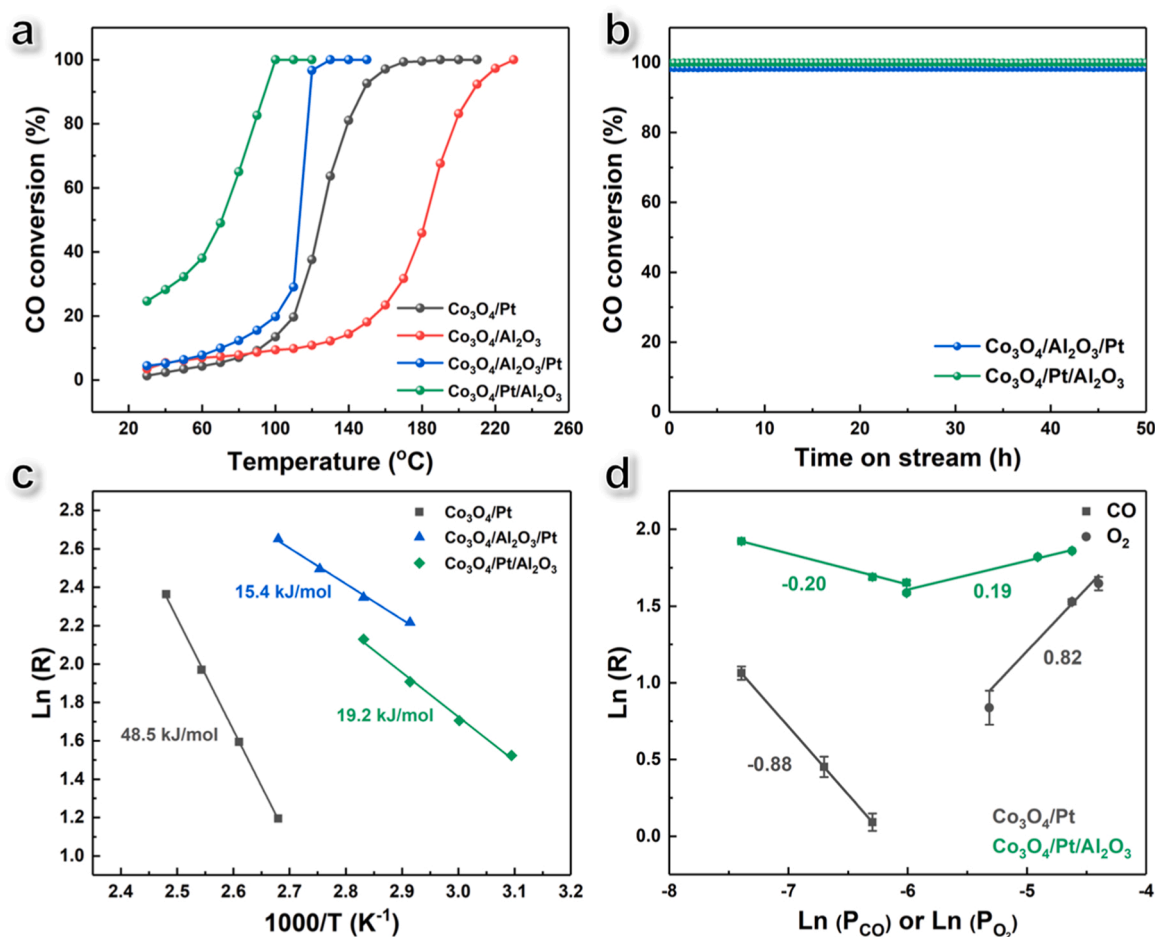
Fig. 5. (a) Temperature-dependent CO conversion over Co_3O_4/Pt, Co_3O_4/Al_2O_3, $Co_3O_4/Al_2O_3/Pt$, and $Co_3O_4/Pt/Al_2O_3$ catalysts, (b) CO conversion of $Co_3O_4/Al_2O_3/Pt$ and $Co_3O_4/Pt/Al_2O_3$ catalysts at 200 °C for 50 h on stream, (c) calculated Arrhenius plots for Co_3O_4/Pt, $Co_3O_4/Al_2O_3/Pt$, $Co_3O_4/Pt/Al_2O_3$ catalysts using CO conversion data below 15%, and (d) the reaction order data of CO and O_2 over Co_3O_4/Pt and $Co_3O_4/Pt/Al_2O_3$ catalysts.

mol). Theoretically, when $ALD-Al_2O_3$ was grown in the outer layer, the active sites of Pt NPs would be covered, which is unfavorable to the penetration of the substrate molecules and leads a poor activity. However, $Co_3O_4/Pt/Al_2O_3$ exhibited good activity in CO oxidation. Combined with the TEM images of $Co_3O_4/Pt/Al_2O_3$, the external $ALD-Al_2O_3$ layer on the catalyst may not be perfect and the active Pt and Co_3O_4 nanoparticles were uniformly distributed around the skeleton, allowing the active sites to contact with the reacting substrate.

Although the Al_2O_3 component is generally known to be inert in CO oxidation reactions, herein, the catalyst activity of Pt was enhanced by the introduction of Al_2O_3 film, which may be due to the electron-modulating effect of Al_2O_3 on Pt NPs (vide infra). Next, the reaction orders with respect to CO and O_2 over Co_3O_4/Pt and $Co_3O_4/Pt/Al_2O_3$ catalysts were calculated to confirm the influence of the Al_2O_3 film. As can be seen in Fig. 5d, the reaction orders of CO on Co_3O_4/Pt and $Co_3O_4/Pt/Al_2O_3$ are − 0.88 and − 0.20, respectively. The lower reaction order of CO suggests a strong binding of CO on Pt NPs at low temperatures [32], leading to the relatively poorer activity of Co_3O_4/Pt, which is the well-known CO poisoning effect. The result also suggests that the $ALD-Al_2O_3$ layer can alleviate this CO-poisoning effect. In addition, the reaction orders of O_2 on Co_3O_4/Pt and $Co_3O_4/Pt/Al_2O_3$ are 0.82 and 0.19, respectively. A lower reaction order of O_2 for $Co_3O_4/Pt/Al_2O_3$ indicates the non-competitive adsorption of CO and O_2 on $Co_3O_4/Pt/Al_2O_3$ and a lower O_2 activation barrier [33,34].

Next, the Pt-containing catalysts were annealed at 500 °C and 600 °C for 5 h in air, respectively, to check the thermal stability of the supported Pt NPs. Fig. 6 displays the shift of the light-off curves before and after the annealing treatment. It was found that Co_3O_4/Pt without $ALD-Al_2O_3$ showed an increased T_{100} to 200 °C after annealing treatment at 500 °C. This characteristic was more pronounced after annealing treatment at 600 °C (T_{100} = 250 °C). Such deactivation was also observed in $Co_3O_4/Al_2O_3/Pt$ where Al_2O_3 was located in the middle layer, but the shift of the light-off curves was insignificant, as compared to the Co_3O_4/Pt catalyst, indicating that the catalytic activity of Pt NPs could also be maintained at high temperatures when Al_2O_3 was in the middle layer. Interestingly, the improved thermal stability of Pt NPs by the $ALD-Al_2O_3$ layer was visualized when the Al_2O_3 layer was coated in the outmost layer (i.e., $Co_3O_4/Pt/Al_2O_3$). For instance, after annealing at 500 °C, the T_{100} of $Co_3O_4/Pt/Al_2O_3$ even decreased from the original 100 °C to 80 °C. The CO conversion over the annealed catalysts was much higher than the fresh catalyst at each tested temperature, which can be attributed to the electron-modulating effect of $ALD-Al_2O_3$ on Pt NPs (vide infra). Although the deactivation characteristic was also observed at 600 °C for $Co_3O_4/Pt/Al_2O_3$, the T_{100} was only increased by 10 °C and the shift of light-off curves was not as pronounced as that of Co_3O_4/Pt, this evidence is a great indication of the improvement of $ALD-Al_2O_3$ on the thermal stability of Pt NPs.

3.3. Characterization of surface chemical states of Pt by XPS analysis

XPS characterization was then performed to analyze the chemical states of Pt on the surface of the catalysts. First, the signals belonging to Pt, Al, Co, O, and C elements can be seen clearly in survey scan spectra (Figs. S4, 5). Considering that the signals of Al *2p* orbitals and Pt *4f*
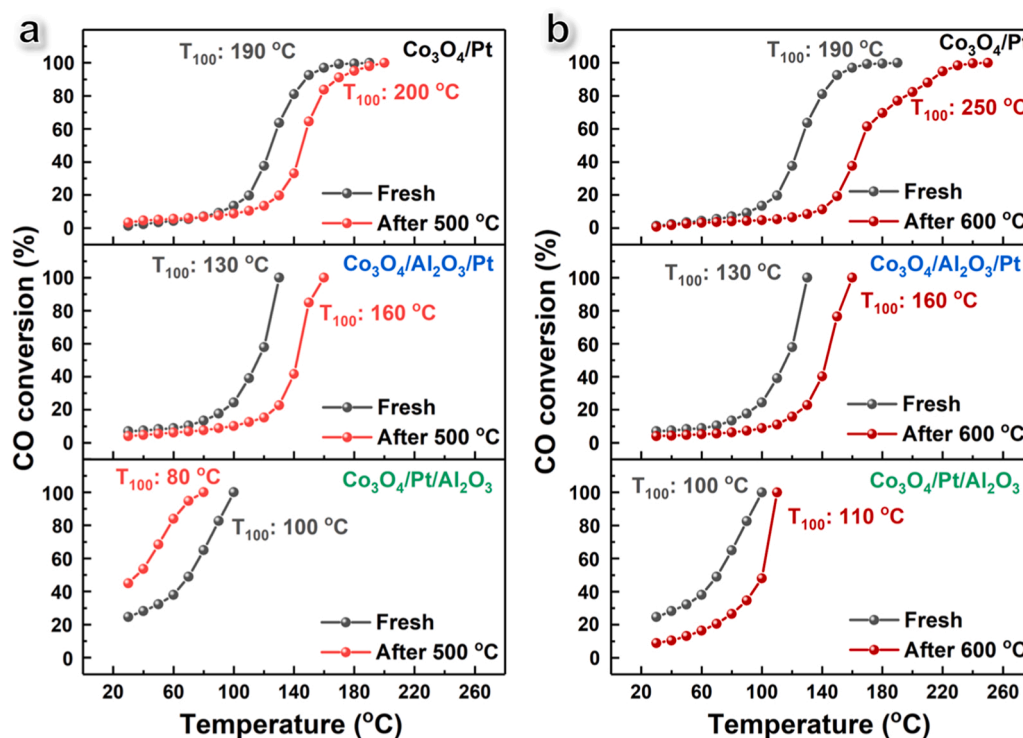
Fig. 6. Comparison of light-off curves for Co_3O_4/Pt, $Co_3O_4/Al_2O_3/Pt$, and $Co_3O_4/Pt/Al_2O_3$ catalysts before and after annealing treatment at 500 °C (a) and 600 °C (b) for 5 h, wherein, the curves of the annealed catalysts are marked in red color and the curves of the fresh catalysts are marked in grey color.

orbitals overlap near the binding energy of ~73 eV, we concentrate on the signals of Pt $4d$ orbitals among catalysts [35]. As shown in Fig. 7a, the $4d$ spectrum of Pt in fresh-prepared Co_3O_4/Pt can be deconvoluted into two peaks, which are attributed to the peaks to Pt^0 (315.0 eV) and Pt^{2+} (317.4 eV), respectively [33]. After annealing in the air at 500 °C for 5 h, the $4d$ signal of Pt can be deconvoluted into a new peak of Pt^{4+} (319.1 eV, Fig. 7d). Meanwhile, the peak intensity of Pt^{2+} increases but Pt^0 decreases, indicating that Pt undergoes significant oxidation with an increase of valence state. This conclusion is also verified by the XPS spectra of Pt $4f$ (Fig. S6). The situation changed when ALD-Al_2O_3 exists in the middle and outer layers. It should be noted that the Pt signal was detected even when ALD-Al_2O_3 film was in the outer layer, which can be attributed to the incomplete encapsulation of Al_2O_3 on Pt. Although the $4d$ signal of Pt in $Co_3O_4/Al_2O_3/Pt$ and $Co_3O_4/Pt/Al_2O_3$ catalysts can also be deconvoluted into two peaks belonging to Pt^0 and Pt^{2+} (Fig. 7b,c), and the peak intensity of Pt^0 did not change as significantly as that of Co_3O_4/Pt catalyst after annealing treatment (Fig. 7e,f), indicating that the ALD-Al_2O_3 film can play an oxidation resistance role during annealing treatment which allows Pt to be oxidized to a smaller degree.

The portions of Pt^0 and $Pt^{\delta+}$ were calculated to further estimate how the Pt^0 content changed after the annealing treatment. These semiquantitative results are shown in Fig. 7g-i. It can be seen that the content of Pt^0 and $Pt^{\delta+}$ in fresh Co_3O_4/Pt was almost half to half, but the content of Pt^0 decreased obviously to 10.6% after annealing treatment (500 °C). While, the fresh $Co_3O_4/Al_2O_3/Pt$ and $Co_3O_4/Pt/Al_2O_3$ catalysts initially preserve a higher amount of Pt^0 (52.1% and 69.3%, respectively). After annealing treatment, the $Co_3O_4/Al_2O_3/Pt$ and $Co_3O_4/Pt/Al_2O_3$ catalysts still retained high content of Pt^0 (36.3% and 40.9%, respectively), which is likely caused by the oxidation resistance effect of ALD-Al_2O_3 film. Due to the higher electronegativity of oxygen, Pt^0 possesses a theoretically stronger affinity for O_2 compared to $Pt^{\delta+}$ [14], which is consistent with our results of reaction order analysis. For instance, the ternary $Co_3O_4/Pt/Al_2O_3$ catalyst possesses more Pt^0, leading to a lower reaction order of O_2 [33], which can well explain the better catalytic activity of the catalysts for CO oxidation.

3.4. Identification of Pt electronic state by in-situ DRIFTS of CO adsorption

The strong adsorption behavior of CO occurring on the Pt surface has been widely used as a probe to identify the Pt site because of its sensitivity to both physical and chemical circumstances [10,36,37]. Therefore, the chemical state of Pt on the catalyst surface was further identified using in-situ DRIFTS [38]. Similarly, we focused on Pt chemical states in fresh-prepared and annealed catalysts (500 °C). As shown in Fig. 8, three IR bands at 2070, 2095, and 2118 cm^{-1} were observed after CO feeding and N_2 purging for 30 min, which can be assigned to the adsorbed CO on different Pt species. For instance, the IR band at 2070 cm^{-1} can be assigned to the linear adsorption of CO on the Pt^0 site [10,39,40]. While the IR bands at ~2097 (2095) and ~2118 cm^{-1} were ascribed to the CO adsorbed on oxidized Pt clusters (Pt_{ox}) and cationic $Pt^{\delta+}$ sites [10,41–43]. In comparison, the Co_3O_4/Al_2O_3 catalyst did not show any IR bands due to CO adsorption (Fig. S7), further verifying that Pt was the dominant site for CO adsorption on the catalyst surface.

Compared with the fresh-prepared Co_3O_4/Pt catalyst, the IR intensities of CO adsorbed on Pt_{ox} and $Pt^{\delta+}$ increased significantly after annealing treatment (Fig. 8d), indicating the oxidation of Pt caused by air. Meanwhile, the intensity of CO adsorbed on Pt^0 was more pronounced for the catalysts with ALD-Al_2O_3 (Fig. 8b,c). One possible reason might be the electronic effect of Al_2O_3 on Pt [41], which will be further confirmed by our DFT calculations (vide infra). In the case of annealed catalysts with ALD-Al_2O_3, the intensity of the IR band belonging to Pt^0 was maintained (Fig. 8e,f), indicating an obvious amount of Pt^0 species in the calcined catalysts. Therefore, both the in-situ DRIFTS results and XPS analysis that the oxidation resistance effect of ALD-Al_2O_3 allows the presence of high amounts of Pt^0 in the catalyst surface even after annealing treatment.
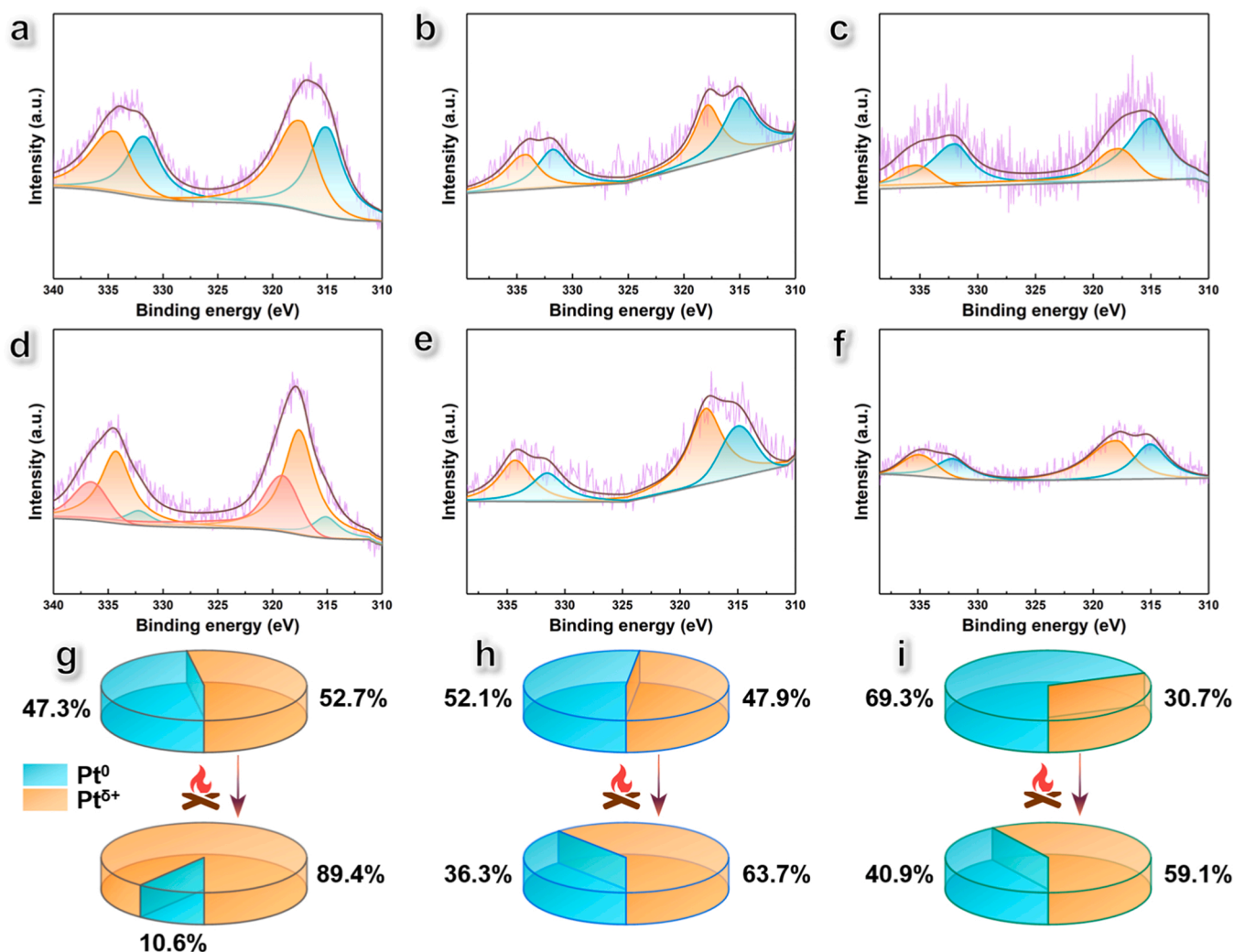
Fig. 7. The deconvolution of Pt *4d* XPS spectra for (a-c) the fresh-prepared catalysts and (d-f) the catalysts after annealing treatment at 500 °C, and (g-i) the estimated semi-quantitative percentage of Pt^0 and $Pt^{\delta+}$ obtained by integrating the corresponding peak.

3.5. Estimation of electron transfer for Pt by DFT calculations

In order to gain insight into how the presence of ALD-Al_2O_3 leads to more amounts of Pt^0, DFT calculations were performed to qualitatively assess how the electron transfer between the Co_3O_4, Al_2O_3, and Pt [44]. According to our XRD characterization data, the most prominent (311) crystal plane of stoichiometric Co_3O_4 was constructed as support [45]. Considering that ALD-Al_2O_3 is amorphous, the common (001) crystal plane surface was chosen to simulate the presence of Al_2O_3 [46,47]. The widely used Pt_5 clusters were placed on the support through the platinum-oxygen bond to simulate the supported catalysts [48,49].

Subsequently, calculations of electron transfer were conducted for the optimized models corresponding to the Co_3O_4/Pt, Co_3O_4/Al_2O_3/Pt, and Co_3O_4/Pt/Al_2O_3 catalysts. As can be seen in Fig. 9, in the case of Co_3O_4/Pt, Pt donated 0.52 electrons to the Co_3O_4 support and the interfacial Pt in contact with Co_3O_4 donated more electrons (Fig. S8), suggesting that the underlying Pt layer in direct contact with the Co_3O_4 support is more likely to exhibit an oxidation state ($Pt^{\delta+}$). This phenomenon is consistent with previous studies [50,51], that is, the electrophilic redox Co_3O_4 tends to gain electrons from Pt, leading to the presence of $Pt^{\delta+}$ in Co_3O_4/Pt [52].

The electron gain and loss states of each Pt atom in the presence of Al_2O_3 can be seen in Figs. S9, 10. Interestingly, Pt gained electrons whether Al_2O_3 exists in the middle or outer layers (+0.96 and +0.38

electrons, Fig. 9b,c) implying a partial reduction of Pt in the presence of Al_2O_3 [53], which are in good agreement with our XPS and in-situ DRIFTS results. It has been mentioned that thin ALD-Al_2O_3 film exhibits special electronic properties in the construction of metal-oxide interfaces, which may be different from the conventional α-Al_2O_3 or γ-Al_2O_3 support [54]. Therefore, we believe that the change of Pt electronic states is achieved by the interactions between Pt and ALD-Al_2O_3 film. Our DFT calculations reveal the reason why a higher amount of Pt^0 species was present in the catalysts with Al_2O_3. The electronic interaction also suggests the Pt clusters were anchored stably on the Co_3O_4 support.

3.6. Reaction mechanism via DFT calculation

The calculation of the reaction pathway based on the optimized DFT model was carried out to investigate the reaction mechanism of CO oxidation. Numerous studies have shown that CO oxidation can be carried out on the Pt sites following the Langmuir-Hinshelwood (LH) mechanism, especially at higher reaction temperatures (>90 °C) [11, 55]. Herein, Pt is considered to be the main active site, but the deposition of Al_2O_3 film in the outer layer will hinder the adsorption and reaction of substrate molecules on Pt during the DFT calculation, which does not match the real experimental observation. Accordingly, we chose the Co_3O_4/Pt and Co_3O_4/Al_2O_3/Pt models to highlight the
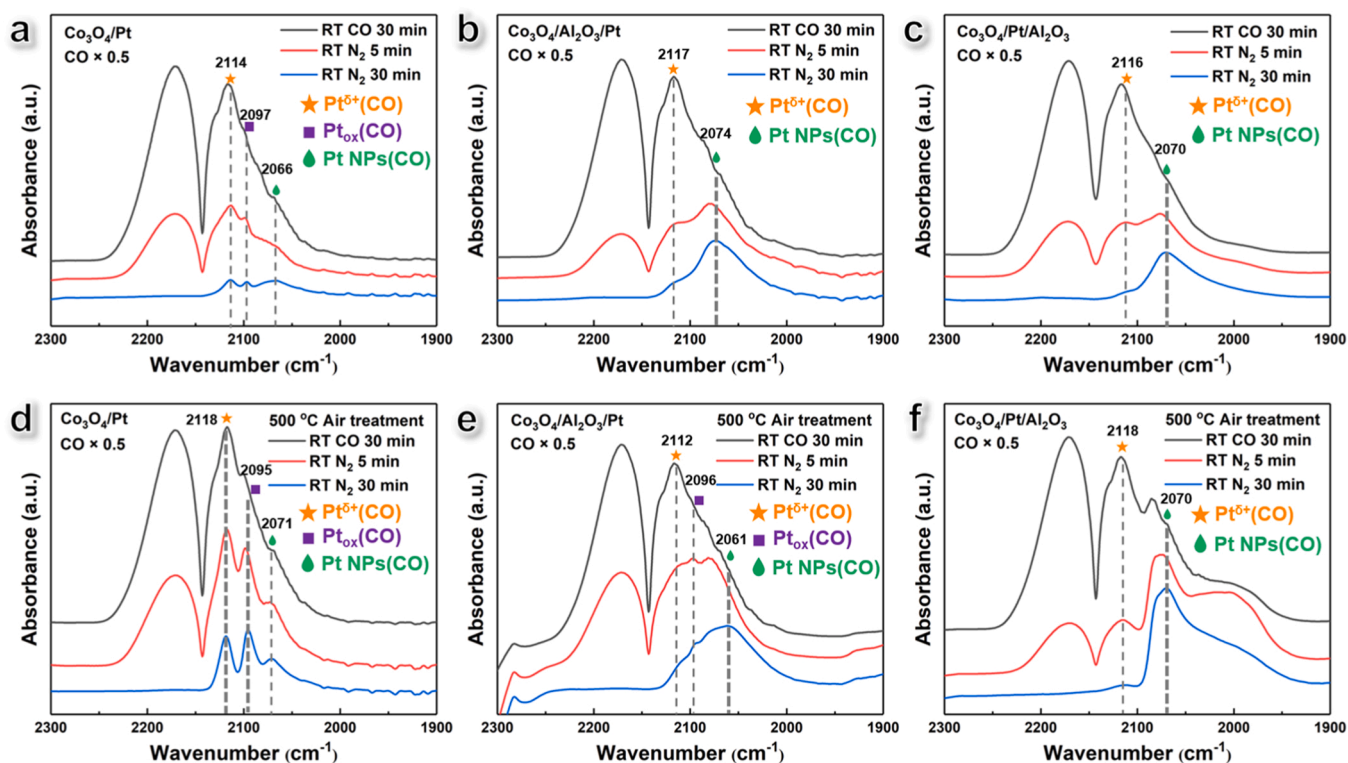
Fig. 8. *In-situ* DRIFTS results of CO feeding, N_2 purging over (a-c) the fresh-prepared catalysts and (d-f) the catalysts after annealing treatment at 500 °C. All the spectra were collected at room temperature (RT).
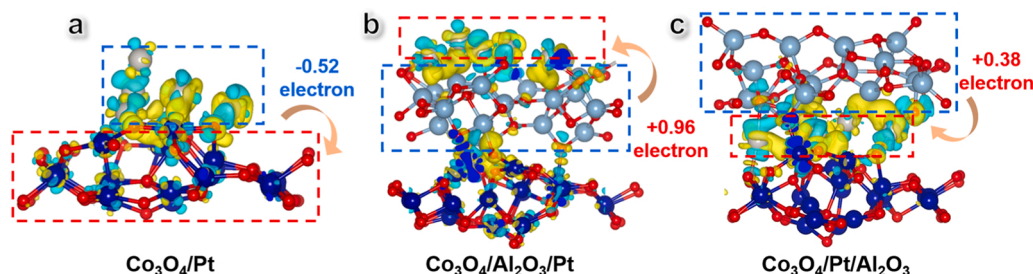

Fig. 9. The atomic models and Bader charge transfer between Pt and Co_3O_4, Al_2O_3 on (a) Co_3O_4/Pt, (b) $Co_3O_4/Al_2O_3/Pt$, and (c) $Co_3O_4/Pt/Al_2O_3$ according to DFT calculations, wherein the yellow electron cloud indicates the increased charge density, and the cyan electron cloud indicates the decreased charge density. Color codes: grey, red, light blue, and navy blue represent Pt, O, Al, and Co atoms, respectively.

beneficial role of Al_2O_3 in the catalytic CO oxidation reaction. The energy barriers and various atomic configurations along the reaction pathways are shown in Fig. 10.

Since oxygen adsorption is critical to CO oxidation, we first calculate the initial step as O_2 adsorption. It was found that $Co_3O_4/Al_2O_3/Pt$ exhibited stronger O_2 adsorption than Co_3O_4/Pt (-0.74 eV to -0.03 eV, step ii). It means that the presence of Al_2O_3 can significantly enhance the adsorption and affinity of the catalyst for O_2, which can be explained by the electronic effect on the Pt site mentioned above. In addition, the O-O bond length of O_2 adsorbed on $Co_3O_4/Al_2O_3/Pt$ is 1.33 Å, which is longer than that of O_2 adsorbed on Co_3O_4/Pt (1.29 Å), reflecting that $Co_3O_4/Al_2O_3/Pt$ possesses a stronger O_2 activation capacity [56]. Then, the CO molecule adsorbed on the same Pt atom with strong binding energies (-1.85 eV to Co_3O_4/Pt and -1.94 eV to $Co_3O_4/Al_2O_3/Pt$, step iii), the state of CO and O_2 co-adsorbed on Pt atom was taken as the initial state of the reaction.

When passed transition state 1 (TS1), the step overcame energy barriers (0.74 eV to Co_3O_4/Pt and 0.41 eV to $Co_3O_4/Al_2O_3/Pt$). Afterward, the CO and O_2 molecules were excited and thus moved closer,

forming carbonate-type *OCOO intermediates, which is a thermodynamically favorable exothermic process (step iv). Afterward, the carbonate-type *OCOO intermediates are further excited, and the O-O band broke after overcoming energy barriers (0.56 eV to Co_3O_4/Pt and 0.11 eV to $Co_3O_4/Al_2O_3/Pt$, TS2). It leads to the release of a CO_2 molecule while leaving an oxygen atom bridgeable bonded to Pt (*OCOO→CO_2 +O*, step v) [57]. In this step, the reaction over $Co_3O_4/Al_2O_3/Pt$ has a larger exothermicity of -1.82 eV than that over Co_3O_4/Pt (-1.56 eV), indicating that the addition of Al_2O_3 makes the reaction easier to occur in thermodynamics. Accordingly, the DFT result demonstrated that the reaction process is thermodynamically and kinetically favorable over $Co_3O_4/Al_2O_3/Pt$, and thus the catalytic oxidation of CO is easier to perform at a lower temperature, which is consistent with our experimental results.

3.7. O_2-TPD characterization and isotope labeling experiments

Besides the LH mechanism, the lattice oxygen in the redox support might also participate in the CO oxidation reaction through the M-vK
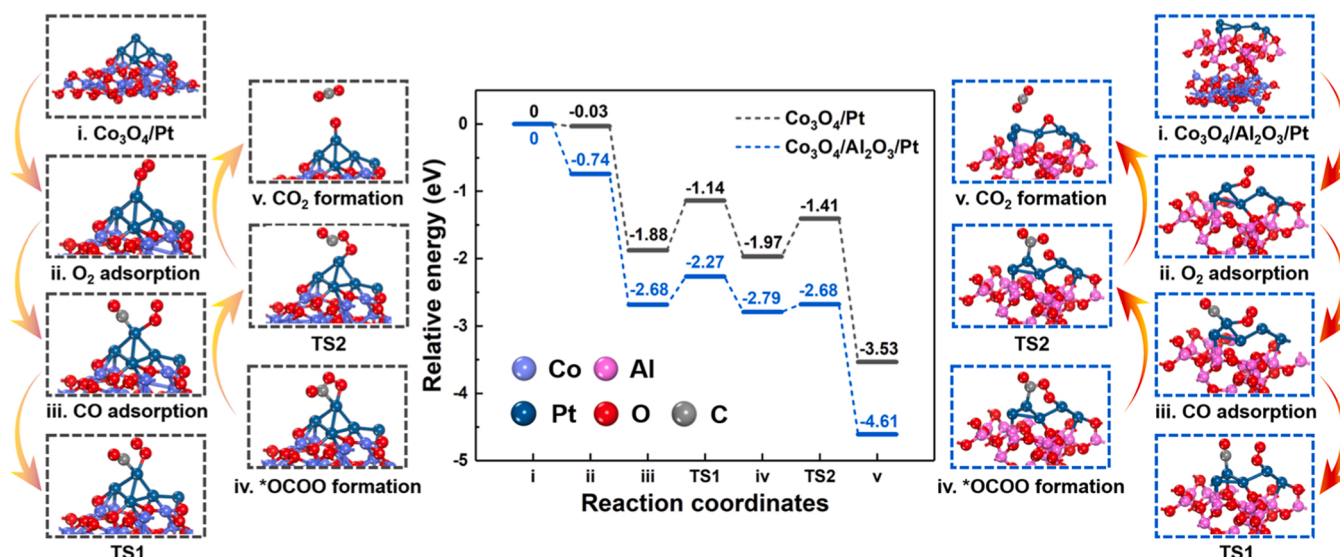
Fig. 10. Calculated reaction pathway for CO oxidation over Co_3O_4/Pt and $Co_3O_4/Al_2O_3/Pt$ catalysts according to the Langmuir-Hinshelwood (LH) mechanism. The data in the profile indicate the relative energy (in eV) of each elementary step, and *OCOO was identified as a reaction intermediate.
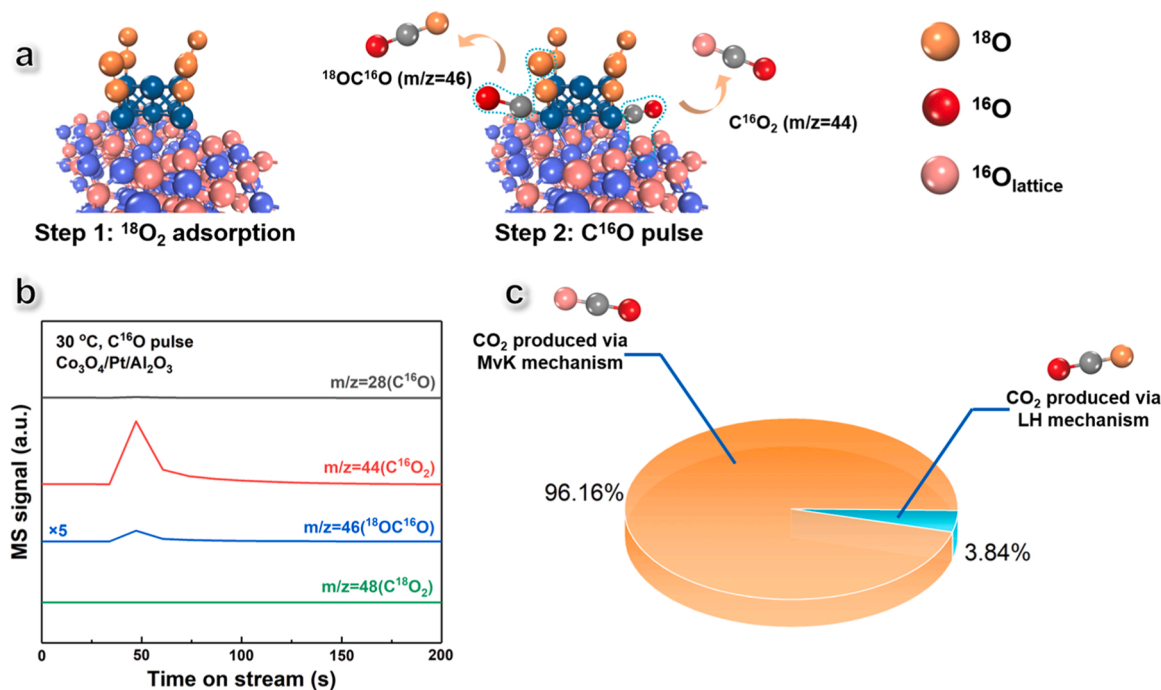

Fig. 11. (a) Schematic diagram of isotope labeling experiments and different reaction mechanisms to produce the different mass-to-charge ratio of CO_2, (b) the real-time signals of $C^{16}O$ ($m/z = 28$), $C^{16}O_2$ ($m/z = 44$), $^{18}OC^{16}O$ ($m/z = 46$), and $C^{18}O_2$ ($m/z = 48$) detected by MS, (c) the contribution percentage of LH mechanism and M-vK mechanism on CO_2 production calculated by integrating the MS signal.

mechanism, particularly in low reaction temperatures [1,48,58]. Considering the support in the present work is redox Co_3O_4, the O_2-TPD test was firstly conducted to investigate the quantity and the mobility of oxygen spices in Co_3O_4/Pt, $Co_3O_4/Al_2O_3/Pt$, and $Co_3O_4/Pt/Al_2O_3$ catalysts. The different oxygen species will be determined from easy to difficult by raising the temperature under the inert atmosphere. As can be seen in Fig. S11, the desorption profiles of oxygen species can be divided into two regions: the region below 250 °C can be attributed to the desorption of adsorbed O_2 (*O_2), and the region from 250 to 500 °C can be attributed to the migration of lattice oxygen (O_{lat}) on the surface of Co_3O_4 [59]. Obviously, $Co_3O_4/Al_2O_3/Pt$ and $Co_3O_4/Pt/Al_2O_3$ have stronger desorption peaks of *O_2 as compared to the catalyst without

ALD-Al_2O_3. In addition, $Co_3O_4/Pt/Al_2O_3$ has lower desorption temperatures of O_{lat} compared to Co_3O_4/Pt and $Co_3O_4/Al_2O_3/Pt$ (339.6 vs. 361.0 and 380.2 °C), indicating that the location of ALD-Al_2O_3 in the outer layer results in a stronger activity of the O_{lat}. The reason may be due to the reduced formation energy of oxygen vacancy (verified by DFT calculations, see Table S5).

To further verify the reactivity of oxygen species in $Co_3O_4/Pt/Al_2O_3$, the isotope labeling experiments were used to quantify the contribution of the M-vK mechanism to CO oxidation at low temperatures (e.g., 30 °C). Specifically, firstly we make the isotope of $^{18}O_2$ adsorbed on the Pt and O_2 adsorption sites, then pulsed a quantitative amount of $C^{16}O$ to the reactor. Since we have demonstrated that the $Co_3O_4/Pt/Al_2O_3$

catalyst possesses activity at room temperature (~20% conversion of CO), the pulsed CO can immediately react with different kinds of oxygen species ($*^{18}O_2$ or O_{lat}) to produce CO_2 with different mass-to-charge ratio and detected by mass spectrometry (Fig. 11a) [60]. The real-time signals of $C^{16}O$ ($m/z = 28$), $C^{16}O_2$ ($m/z = 44$), $^{18}OC^{16}O$ ($m/z = 46$), and $C^{18}O_2$ ($m/z = 48$) were recorded in Fig. 11b. No significant CO signal was observed, suggesting that part of pulsed CO was either converted to CO_2 or adsorbed on Pt. As shown in Fig. 11c, $C^{16}O_2$ ($m/z = 44$) generated by the interaction of CO with O_{lat} through the M-vK mechanism contributes most of the CO_2 production, and the $*O_2$ does not participate significantly in the reaction (weak signal of $m/z = 46$), indicating the physically adsorbed O_2 may not be reactive at the studied temperature. It is believed that the O_{lat}-mediated M-vK mechanism dominates the CO oxidation reaction over the $Co_3O_4/Pt/Al_2O_3$ catalyst at 30 °C (reaches 96.2% of the total CO_2 production). We speculate that the release of O_{lat} from the Co_3O_4 will create oxygen vacancies, and the chemisorbed O_2 adsorbed on the oxygen vacancies possess good reactivity for CO oxidation to form CO_2 to reach a dynamic equilibrium of consumption and replenishment [58].

4. Conclusion

CO oxidation is one of the simplest but most important reactions in both fundamental research and industrial applications, and the catalytic performance strongly depends on the catalyst composition and surface chemistry. The advancement of surface technology and computational chemistry provides us with the opportunity and a broad picture to identify the states of Pt in different catalyst systems. Herein, a series of supported Co_3O_4/Pt catalysts were fabricated by using ZIF-67 as sacrificial templates. The ternary $Co_3O_4/Pt/Al_2O_3$ integrated catalysts were further fabricated to tune the electronic properties of Pt NPs by the ALD-deposited Al_2O_3 films. Whether the Al_2O_3 was located in the middle or outer layer of Pt NPs, it can enhance the catalytic performance in CO catalytic oxidation. One of the best performing $Co_3O_4/Pt/Al_2O_3$ catalysts can completely convert CO to CO_2 at 100 °C with a low activation energy of 15.4 kJ/mol, which also showed great durability at a long time of 50 h. Even after annealing treatment at 500 °C, XPS and in-situ DRIFTS results showed that the $Co_3O_4/Al_2O_3/Pt$ and $Co_3O_4/Pt/Al_2O_3$ catalysts still retained high content of Pt^0 (36.3% and 40.9%, respectively), which can be attributed to the oxidation resistance effect of ALD-Al_2O_3 film. The higher amounts of Pt^0 allow the catalysts to possess stronger oxygen affinity which benefited the CO oxidation performance. Therefore, the annealed $Co_3O_4/Pt/Al_2O_3$ catalysts at 500 or 600 °C did not lose catalytic activity as compared to the fresh catalyst. The underlying reaction mechanism was studied by DFT calculation which confirmed that $Co_3O_4/Al_2O_3/Pt$ exhibited stronger O_2 adsorption than Co_3O_4/Pt (−0.74 vs. −0.03 eV). When passed the two transition states, the energy barriers of $Co_3O_4/Al_2O_3/Pt$ were remarkably lower than those of Co_3O_4/Pt (TS1: 0.41 vs. 0.74 eV and TS2: 0.11 vs. 0.56 eV).

In light of the above findings, our study provides new insight into the regulation of the electronic states of noble metals by using the ALD technique, which may also be extended to other atomically controlled methods such as physical vapor deposition (PVD) and chemical vapor deposition (CVD). Our work not only elucidates the structure-activity relationship between the electronic state of Pt catalysts and CO oxidation activity but also provides a new type of economic Pt catalysts with good performance and reliability for industrial applications such as methanol synthesis, automotive catalysis, PROX in PEMFC, etc.

CRediT authorship contribution statement

Siyuan Hu: Investigation, Methodology, Data analysis, Writing – original draft. **Mingzhen Huang**: Investigation, Methodology. **Jingru Li**: Investigation and Methodology. **Jinxin He**: Investigation and Methodology. **Kaiji Xu**: Methodology. **Xiaoping Rao**: Writing – review & editing. **Dongren Cai**: Writing – review & editing. **Guowu Zhan**:

Writing – review & editing, Supervision, Conceptualization. All authors discussed the results and confirmed the manuscript.

Declaration of Competing Interest

The authors declare that they have no known competing financial interests or personal relationships that could have appeared to influence the work reported in this paper.

Data Availability

Data will be made available on request.

Acknowledgments

Appendix A. Supporting information

Supplementary data associated with this article can be found in the online version at doi:10.1016/j.apcatb.2023.122804.

References

[1] H. Kersell, Z. Hooshmand, G. Yan, D. Le, H. Nguyen, B. Eren, C.H. Wu, I. Waluyo, A. Hunt, S. Nemšák, G. Somorjai, T.S. Rahman, P. Sautet, M. Salmeron, CO oxidation mechanisms on CoO$_x$-Pt thin films, J. Am. Chem. Soc. 142 (2020) 8312–8322.

[2] C.H. Wu, C. Liu, D. Su, H.L. Xin, H.-T. Fang, B. Eren, S. Zhang, C.B. Murray, M. B. Salmeron, Bimetallic synergy in cobalt-palladium nanocatalysts for CO oxidation, Nat. Catal. 2 (2018) 78–85.

[3] W. Yuan, B. Zhu, K. Fang, X.-Y. Li, T.W. Hansen, Y. Ou, H. Yang, J.B. Wagner, Y. Gao, Y. Wang, Z. Zhang, In situ manipulation of the active Au-TiO2 interface with atomic precision during CO oxidation, Science 371 (2021) 517–521.

[4] Y. Zhai, D. Pierre, R. Si, W. Deng, P. Ferrin, U. Nilekar Anand, G. Peng, A. Herron Jeffrey, C. Bell David, H. Saltsburg, M. Mavrikakis, M. Flytzani-Stephanopoulos, Alkali-stabilized Pt-OH$_x$ species catalyze low-temperature water-gas shift reactions, Science 329 (2010) 1633–1636.

[5] X. Zhang, M. Zhang, Y. Deng, M. Xu, L. Artiglia, W. Wen, R. Gao, B. Chen, S. Yao, X. Zhang, M. Peng, J. Yan, A. Li, Z. Jiang, X. Gao, S. Cao, C. Yang, A.J. Kropf, J. Shi, J. Xie, M. Bi, J.A. van Bokhoven, Y.-W. Li, X. Wen, M. Flytzani-Stephanopoulos, C. Shi, W. Zhou, D. Ma, A stable low-temperature H$_2$-production catalyst by crowding Pt on α-MoC, Nature 589 (2021) 396–401.

[6] J.T. Kummer, Catalysts for automobile emission control, Prog. Energy Combust. Sci. 6 (1980) 177–199.

[7] R. Huang, K. Kim, H.J. Kim, M.G. Jang, J.W. Han, Size-controlled Pd nanoparticles loaded on Co$_3$O$_4$ nanoparticles by calcination for enhanced CO oxidation, ACS Appl. Nano Mater. 3 (2019) 486–495.

[8] R. Rangel, E. González-A, A. Solís-García, T.A. Zepeda, D.H. Galván, A. Gómez-Cortés, G. Díaz, Pt and Ir supported on mixed Ce0.97Ru0.03O2 oxide as low-temperature CO oxidation catalysts, Catal. Today 392–393 (2022) 3–12.

[9] A. Beniya, S. Higashi, Towards dense single-atom catalysts for future automotive applications, Nat. Catal. 2 (2019) 590–602.

[10] K. Ding, A. Gulec, A.M. Johnson, N.M. Schweitzer, G.D. Stucky, L.D. Marks, P. C. Stair, Identification of active sites in CO oxidation and water-gas shift over supported Pt catalysts, Science 350 (2015) 189–192.

[11] Q. Wang, J. Gong, H. Zhang, Q.-Y. Fan, L. Xue, J. Wu, J. Li, Y. Wang, Z. Liu, R. Gao, S. Zeng, Co-promotion of two-type active sites: PtCu$_x$ single-atom alloy and copper-ceria interface for preferential oxidation of CO, Appl. Catal., B 306 (2022) 121117.

[12] X. Zhao, Y. Hu, H. Jiang, J. Yu, R. Jiang, C. Li, Engineering TiO2 supported Pt Sub-nanoclusters via introducing variable valence Co Ion in high-temperature flame for CO oxidation, Nanoscale 10 (2018) 13384–13392.

[13] T.W. van Deelen, C. Hernández Mejía, K.P. de Jong, Control of metal-support interactions in heterogeneous catalysts to enhance activity and selectivity, Nat. Catal. 2 (2019) 955–970.

[14] A. Beniya, S. Higashi, N. Ohba, R. Jinnouchi, H. Hirata, Y. Watanabe, CO oxidation activity of non-reducible oxide-supported mass-selected few-atom Pt single-clusters, Nat. Commun. 11 (2020) 1888.

[15] W. Zhu, Z. Wu, G.S. Foo, X. Gao, M. Zhou, B. Liu, G.M. Veith, P. Wu, K.L. Browning, H.N. Lee, H. Li, S. Dai, H. Zhu, Taming interfacial electronic properties of platinum

nanoparticles on vacancy-abundant boron nitride nanosheets for enhanced catalysis, Nat. Commun. 8 (2017) 15291.

[16] Y.P.G. Chua, G.T.K.K. Gunasooriya, M. Saeys, E.G. Seebauer, Controlling the CO oxidation rate over Pt/TiO$_2$ catalysts by defect engineering of the TiO$_2$ support, J. Catal. 311 (2014) 306–313.

[17] Y.-Z. Chen, Z.U. Wang, H. Wang, J. Lu, S.-H. Yu, H.-L. Jiang, Singlet oxygen-engaged selective photo-oxidation over Pt nanocrystals/porphyrinic MOF: the roles of photothermal effect and Pt electronic state, J. Am. Chem. Soc. 139 (2017) 2035–2044.

[18] Y. Zhou, D.E. Doronkin, M. Chen, S. Wei, J.-D. Grunwaldt, Interplay of Pt and crystal facets of TiO$_2$: CO oxidation activity and operando XAS/DRIFTS studies, ACS Catal. 6 (2016) 7799–7809.

[19] R. Aso, H. Hojo, Y. Takahashi, T. Akashi, Y. Midoh, F. Ichihashi, H. Nakajima, T. Tamaoka, K. Yubuta, H. Nakanishi, H. Einaga, T. Tanigaki, H. Shinada, Y. Murakami, Direct identification of the charge state in a single platinum nanoparticle on titanium oxide, Science 378 (2022) 202–206.

[20] G.-F. Zhou, J. Ma, S. Bai, L. Wang, Y. Guo, CO catalytic oxidation over Pd/CeO$_2$ with different chemical states of Pd, Rare Met. 39 (2020) 800–805.

[21] A. Henning, J.D. Bartl, A. Zeidler, S. Qian, O. Bienek, C.-M. Jiang, C. Paulus, B. Rieger, M. Stutzmann, I.D. Sharp, Aluminum oxide at the monolayer limit via oxidant-free plasma-assisted atomic layer deposition on GaN, Adv. Funct. Mater. 31 (2021) 2101441.

[22] H. Yang, D. Xiang, H. Mao, T. Liu, Y. Wang, R. Guo, Y. Zheng, X. Ye, J. Gao, Q. Ge, C. Deng, W. Cai, X. Zhang, S. Qin, W. Chen, Native oxide seeded spontaneous integration of dielectrics on exfoliated black phosphorus, ACS Appl. Mater. Interfaces 12 (2020) 24411–24418.

[23] X. Liang, J. Li, M. Yu, C.N. McMurray, J.L. Falconer, A.W. Weimer, Stabilization of supported metal nanoparticles using an ultrathin porous shell, ACS Catal. 1 (2011) 1162–1165.

[24] S. Lee, C. Lin, S. Kim, X. Mao, T. Kim, S.-J. Kim, R.J. Gorte, W. Jung, Manganese oxide overlayers promote CO oxidation over Pt, ACS Catal. 11 (2021) 13935–13946.

[25] Z. Huang, L. Fan, F. Zhao, B. Chen, K. Xu, S.-F. Zhou, J. Zhang, Q. Li, D. Hua, G. Zhan, Rational engineering of multilayered Co$_3$O$_4$/ZnO nanocatalysts through chemical transformations from matryoshka-Type ZIFs, Adv. Funct. Mater. 29 (2019) 1903774.

[26] G. Zhan, H.C. Zeng, ZIF-67-derived nanoreactors for controlling product selectivity in CO$_2$ hydrogenation, ACS Catal. 7 (2017) 7509–7519.

[27] G. Kresse, J. Furthmüller, Efficient iterative schemes for Ab initio total-energy calculations using a plane-wave basis set, Phys. Rev. B 54 (1996) 11169–11186.

[28] J.P. Perdew, K. Burke, M. Ernzerhof, Generalized gradient approximation made simple, Phys. Rev. Lett. 77 (1996) 3865–3868.

[29] G. Henkelman, B.P. Uberuaga, H. Jónsson, A. Climbing, Image nudged elastic band method for finding saddle points and minimum energy paths, J. Chem. Phys. 113 (2000) 9901–9904.

[30] N. Justh, B. Berke, K. László, L.P. Bakos, A. Szabó, K. Hernádi, I.M. Szilágyi, Preparation of graphene oxide/semiconductor oxide composites by using atomic layer deposition, Appl. Surf. Sci. 453 (2018) 245–251.

[31] T. Diemant, J. Bansmann, CO oxidation on planar Au/TiO$_2$ model catalysts under realistic conditions: a combined kinetic and IR study, ChemPhysChem 22 (2021) 542–552.

[32] S.B. Vendelbo, C.F. Elkjær, H. Falsig, I. Puspitasari, P. Dona, L. Mele, B. Morana, B. J. Nelissen, R. van Rijn, J.F. Creemer, P.J. Kooyman, S. Helveg, Visualization of oscillatory behaviour of Pt nanoparticles catalysing CO oxidation, Nat. Mater. 13 (2014) 884–890.

[33] X. Liu, Q. Zhu, Y. Lang, K. Cao, S. Chu, B. Shan, R. Chen, Oxide-nanotrap-anchored platinum nanoparticles with high activity and sintering resistance by area-selective atomic layer deposition, Angew. Chem. Int. Ed. 56 (2017) 1648–1652.

[34] W. Wang, D. Li, H. Yu, C. Liu, C. Tang, J. Chen, J. Lu, M. Luo, Insights into different reaction behaviors of propane and CO oxidation over Pt/CeO$_2$ and Pt/Nb$_2$O$_5$: the crucial roles of support properties, J. Phys. Chem. C. 125 (2021) 19301–19310.

[35] K. Cheng, L.C.J. Smulders, L.I. van der Wal, J. Oenema, J.D. Meeldijk, N.L. Visser, G. Sunley, T. Roberts, Z. Xu, E. Doskocil, H. Yoshida, Y. Zheng, J. Zečević, P.E. de Jongh, K.P. de Jong, Maximizing noble metal utilization in solid catalysts by control of nanoparticle location, Science 377 (2022) 204–208.

[36] T. Bauer, S. Maisel, D. Blaumeiser, J. Vecchietti, N. Taccardi, P. Wasserscheid, A. Bonivardi, A. Görling, J. Libuda, Operando DRIFTS and DFT study of propane dehydrogenation over solid- and liquid-supported Ga$_x$Pt$_y$ catalysts, ACS Catal. 9 (2019) 2842–2853.

[37] N. Podda, M. Corva, F. Mohamed, Z. Feng, C. Dri, F. Dvořák, V. Matolín, G. Comelli, M. Peressi, E. Vesselli, Experimental and theoretical investigation of the restructuring process induced by CO at near ambient pressure: Pt nanoclusters on graphene/Ir(111), ACS Nano 11 (2017) 1041–1053.

[38] L. Fan, K. Wang, K. Xu, Z. Liang, H. Wang, S.F. Zhou, G. Zhan, Structural isomerism of two Ce-BTC for fabricating Pt/CeO$_2$ nanorods toward low-temperature CO oxidation, Small 16 (2020) e2003597.

[39] Y. Chen, Y. Feng, L. Li, J. Liu, X. Pan, W. Liu, F. Wei, Y. Cui, B. Qiao, X. Sun, X. Li, J. Lin, S. Lin, X. Wang, T. Zhang, Identification of active sites on high-performance Pt/Al$_2$O$_3$ catalyst for cryogenic CO oxidation, ACS Catal. 10 (2020) 8815–8824.

[40] A. Sattler, M. Paccagnini, M.P. Lanci, S. Miseo, C.E. Kliewer, Platinum catalyzed C-H activation and the effect of metal-support interactions, ACS Catal. 10 (2020) 710–720.

[41] M.J. Kale, P. Christopher, Utilizing quantitative in situ FTIR spectroscopy to identify well-coordinated Pt atoms as the active site for CO oxidation on Al$_2$O$_3$-supported Pt catalysts, ACS Catal. 6 (2016) 5599–5609.

[42] K. Murata, N. Kurimoto, Y. Yamamoto, A. Oda, J. Ohyama, A. Satsuma, Structure-property relationships of Pt-Sn nanoparticles supported on Al$_2$O$_3$ for the dehydrogenation of methylcyclohexane, ACS Appl. Nano Mater. 4 (2021) 4532–4541.

[43] L. DeRita, S. Dai, K. Lopez-Zepeda, N. Pham, G.W. Graham, X. Pan, P. Christopher, Catalyst architecture for stable single atom dispersion enables site-specific spectroscopic and reactivity measurements of CO adsorbed to Pt atoms, oxidized pt clusters, and metallic Pt clusters on TiO$_2$, J. Am. Chem. Soc. 139 (2017) 14150–14165.

[44] G. Henkelman, A. Arnaldsson, H. Jónsson, A. Fast, Robust algorithm for bader decomposition of charge density, Comput. Mater. Sci. 36 (2006) 354–360.

[45] Z. Deng, C. Ma, Z. Li, Y. Luo, L. Zhang, S. Sun, Q. Liu, J. Du, Q. Lu, B. Zheng, X. Sun, High-Efficiency Electrochemical Nitrate Reduction to Ammonia on a Co$_3$O$_4$ Nanoarray Catalyst with Cobalt Vacancies, ACS Appl. Mater. Interfaces 14 (2022) 46595–46602.

[46] A.A. Tamijani, J.L. Bjorklund, L.J. Augustine, J.G. Catalano, S.E. Mason, Density Functional Theory and Thermodynamics Modeling of Inner-Sphere Oxyanion Adsorption on the Hydroxylated α-Al$_2$O$_3$(001) Surface, Langmuir 36 (2020) 13166–13180.

[47] M.J. DelloStritto, S.M. Piontek, M.L. Klein, E. Borguet, Effect of Functional and Electron Correlation on the Structure and Spectroscopy of the Al$_2$O$_3$(001)-H$_2$O Interface, J. Phys. Chem. Lett. 10 (2019) 2031–2036.

[48] S. Kaiser, F. Maleki, K. Zhang, W. Harbich, U. Heiz, S. Tosoni, B.A.J. Lechner, G. Pacchioni, F. Esch, Cluster Catalysis with Lattice Oxygen: Tracing Oxygen Transport from a Magnetite (001) Support onto Small Pt Clusters, ACS Catal. 11 (2021) 9519–9529.

[49] K. Kuge, K. Yamauchi, K. Sakai, Theoretical Study on the Mechanism of the Hydrogen Evolution Reaction Catalyzed by Platinum Subnanoclusters, Dalton Trans. 52 (2023) 583–597.

[50] Y. Lykhach, F. Faisal, T. Skála, A. Neitzel, N. Tsud, M. Vorokhta, F. Dvořák, K. Beranová, Y. Kosto, K.C. Prince, V. Matolín, J. Libuda, Interplay between the Metal-support Interaction and Stability in Pt/Co$_3$O$_4$(111) Model Catalysts, J. Mater. Chem. A 6 (2018) 23078–23086.

[51] F. Faisal, M. Bertram, C. Stumm, T. Wähler, R. Schuster, Y. Lykhach, A. Neitzel, T. Skála, N. Tsud, K. Beranová, K.C. Prince, V. Matolín, O. Brummel, J. Libuda, Electrocatalysis with Atomically Defined Model Systems: Metal-Support Interactions between Pt Nanoparticles and Co$_3$O$_4$(111) under Ultrahigh Vacuum and in Liquid Electrolytes, J. Phys. Chem. C. 122 (2018) 20787–20799.

[52] L. Li, M. Wei, F. Chen, W. Ji, Pt-Embedded-Co$_3$O$_4$ Hollow Structure as a Highly Efficient Catalyst for Toluene Combustion, Catal. Sci. Technol. 11 (2021) 5491–5497.

[53] V.T.T. Ho, C.-J. Pan, J. Rick, W.-N. Su, B.-J. Hwang, Nanostructured Ti0.7Mo0.3O2 Support Enhances Electron Transfer to Pt: High-Performance Catalyst for Oxygen Reduction Reaction, J. Am. Chem. Soc. 133 (2011) 11716–11724.

[54] B. Zhang, Y. Qin, Interface Tailoring of Heterogeneous Catalysts by Atomic Layer Deposition, ACS Catal. 8 (2018) 10064–10081.

[55] M.A. van Spronsen, J.W.M. Frenken, I.M.N. Groot, Surface Science under Reaction Conditions: CO Oxidation on Pt and Pd Model Catalysts, Chem. Soc. Rev. 46 (2017) 4347–4374.

[56] X. Yu, C. Zhao, T. Zhang, Z. Liu, Molecular and Dissociative O$_2$ Adsorption on the Cu$_2$O(111) Surface, Phys. Chem. Chem. Phys. 20 (2018) 20352–20362.

[57] S. Wang, Z. Yang, X. Chu, W. Wang, Design of Efficient Catalysts for CO Oxidation on Titanium Carbide-Supported Platinum via Computational Study, J. Phys. Chem. C. 122 (2018) 25974–25982.

[58] Y. Lu, S. Zhou, C.-T. Kuo, D. Kunwar, C. Thompson, A.S. Hoffman, A. Boubnov, S. Lin, A.K. Datye, H. Guo, A.M. Karim, Unraveling the Intermediate Reaction Complexes and Critical Role of Support-Derived Oxygen Atoms in CO Oxidation on Single-Atom Pt/CeO$_2$, ACS Catal. 11 (2021) 8701–8715.

[59] W. Tang, W. Xiao, S. Wang, Z. Ren, J. Ding, P.-X. Gao, Boosting Catalytic Propane Oxidation over PGM-free Co$_3$O$_4$ Nanocrystal Aggregates Through Chemical Leaching: A Comparative Study with Pt and Pd Based Catalysts, Appl. Catal., B 226 (2018) 585–595.

[60] A. Beniya, K. Miwa, Y. Hirata, S. Watanabe, S. Higashi, Insight for Designing Mass-Efficient Metal-Oxide-Supported Heterogeneous Catalyst from the Identification of the Catalytically Active Edge Sites Using Isotopically Labeled ^{13}CO and ^{18}O$_2$, ACS Catal. 12 (2022) 1977–1985.